



Exploring time-resolved photoluminescence for nanowires using a three-dimensional computational transient model

Journal:	<i>Nanoscale</i>
Manuscript ID	NR-ART-03-2018-001908
Article Type:	Paper
Date Submitted by the Author:	06-Mar-2018
Complete List of Authors:	<p>Ren, Dingkun; University of California Los Angeles, Electrical and Computer Engineering Scofield, Adam C.; University of California Los Angeles, Electrical and Computer Engineering Farrell, Alan C.; University of California Los Angeles, Electrical and Computer Engineering Rong, Zixuan; University of California Los Angeles, Electrical and Computer Engineering Haddad, Michael A.; University of California Los Angeles, Electrical and Computer Engineering Laghumavarapu, Ramesh; University of California Los Angeles, Electrical and Computer Engineering Liang, Bao; University of California Los Angeles, California Nanosystems Institute Huffaker, Diana; University of California Los Angeles, Electrical and Computer Engineering; University of California Los Angeles, Electrical and Computer Engineering; Cardiff University, School of Physics and Astronomy</p>

Exploring Time-Resolved Photoluminescence for Nanowires Using a Three-dimensional Computational Transient Model

Dingkun Ren,^{*a} Adam C. Scofield,^a Alan C. Farrell,^a Zixuan Rong,^a Michael A. Haddad,^a
Ramesh B. Laghumavarapu,^a Baolai Liang^b and Diana L. Huffaker^{a,b,c}

^a*Department of Electrical and Computer Engineering, University of California at Los Angeles,
Los Angeles, California 90095, USA*

^b*California NanoSystems Institute, University of California at Los Angeles, Los Angeles,
California 90095, USA*

^c*School of Physics and Astronomy, Cardiff University, Cardiff, Wales CF24 3AA, UK*

KEYWORDS

TRPL, nanowires, transient, modeling, carrier lifetime, GaAs on Si, heterointerfaces

ABSTRACT

Time-resolved photoluminescence (TRPL) has been implemented experimentally to measure the carrier lifetime of semiconductors for decades. For the characterization of nanowires, the rich information embedded in TRPL curves has not been fully interpreted and meaningfully mapped to the respective material properties. This is because their three-dimensional (3-D) geometries result in more complicated mechanisms of carrier recombination than those in thin films and analytical solutions cannot be found for those nanostructures. In this work, we extend the intrinsic power of TRPL by developing a full 3-D transient model, which accounts for different material properties and drift-diffusion, to simulate TRPL curves for nanowires. To show the capability of the model, we performed TRPL measurements on a set of GaAs nanowire arrays grown on silicon substrates and then fit the measured data by tuning various material properties, including carrier mobility, Shockley-Read-Hall recombination lifetime, and surface recombination velocity at the GaAs-Si heterointerface. From the resultant TRPL simulations, we numerically identify the lifetime characteristics of those material properties. In addition, we computationally map the spatial and temporal electron distributions in nanowire segments and reveal the underlying carrier dynamics. We believe this study provides a theoretical foundation for interpretation of TRPL measurements to unveil the complex carrier recombination mechanisms in 3-D nanostructured materials.

Introduction

The bottom-up growth of vertical nanowires enables heteroepitaxy with large lattice mismatch due to elastic deformation occurring at heterogeneous interfaces.^{1,2} This capability leads to the integration of III-V nanowire-based electrical and optical devices on silicon platforms, including field-effect transistors,³⁻⁵ lasers,⁶⁻⁹ light-emitting diodes,¹⁰⁻¹⁸ photodetectors,^{19,20} and solar cells.²¹⁻²⁶ To develop those devices with high performance, it is important to explore material properties and understand carrier dynamics in nanowires. However, the characterization of nanowires is challenging, much more so than that of thin films. This is because the three-dimensional (3-D) geometries of nanowires have much larger surface-to-volume ratios and smaller cross-sections at the nanowire-substrate heterointerfaces, and therefore analytical solutions cannot be found for such nanostructures.

Over the last decade, remarkable advances in material characterization have taken place, enabling the study of the material properties and carrier dynamics of III-V (or Si) nanowires. A commonly used contactless optical probing technique known as time-resolved photoluminescence (TRPL) measures the temporal decay of radiative recombination and interprets carrier lifetime that reflects the dynamic process of carriers and intrinsic recombination mechanisms. For example, lifetime measurements of GaAs nanowires grown on Si have been attempted to explore trap-induced nonradiative recombination and twinning under various growth conditions and to study surface passivation by introducing an AlGaAs shell.^{23,27-29} Unfortunately, the real-time motion of carriers has not been interpreted, and the interaction of carriers with heterointerfaces and local defects remains unclear. Alternatively, time-resolved THz spectroscopy (also called “optical pump-THz probe”) is able to observe relative changes of nanowire trap density and carrier mobility by fitting to analytical equations.³⁰⁻³³ Furthermore, spatially-separated femtosecond pump-probe microscopy is capable of imaging the temporal migration of carriers in individual nanowires with picosecond temporal resolution, which has been implemented to study diameter-dependent carrier lifetime and recombination mechanisms in Si nanowires.³⁴⁻³⁷ However, neither spectroscopy technique is capable of extracting information at the nanowire-substrate interface since

nanowires need to be mechanically transferred onto quartz substrates because of either absorption in semiconductor substrates in the THz regime or limitations of the experimental setup. To accurately characterize nanowire properties, which is critical to the development of high-performance devices, the nanowire-substrate interface needs to be included. A probing technique called two-photon optical-beam-induced current (TOBIC) has been applied to map 3-D photocurrent current responses for free-standing GaAs photovoltaics grown on GaAs substrates.³⁸ Still, it has not been adopted to reconstruct the real-time carrier transport or extract multiple material properties.

Although TRPL is traditionally used to measure carrier lifetimes and infer recombination mechanisms, we believe the rich physics underlying TRPL can be harnessed to concurrently explore multiple material properties that reflect the complex carrier dynamics in III-V nanowires with nanowire-substrate heterointerfaces. This is because the overall lifetime is influenced by the carrier dynamics resulting from not only one but multiple mechanisms. In other words, the lifetime and material properties of a nanowire are related, but not in a simple one-to-one correlation, and this is mainly due to the fact that the carrier motion is in a 3-D space. Since changing only one of these mechanisms is experimentally impractical, we develop a 3-D TRPL transient model and take a simulation approach to investigate the correlation between lifetime and material properties for nanowires. Without losing generality, we consider three important material properties, namely, mobility (μ), Shockley-Read-Hall (SRH) recombination lifetime (τ_{SRH}), and nanowire-substrate heterointerface recombination velocity (S_n). To validate the model and demonstrate the concept, we study the case of p-type GaAs nanowires on silicon substrates. We measured the minority (electron) carrier lifetime (τ_n) of p-type GaAs nanowires by TRPL and performed numerical simulations to fit the measured TRPL curves. By tuning the material properties of GaAs nanowire segments as well as GaAs seeding layers, we study the impact of those properties on τ_n and further identified their lifetime characteristics. Finally, we tabulate the values of material properties based on the simulation results and interpret the carrier dynamics by mapping spatial electron distribution as a function of time. Note that we used patterned selective-area epitaxy (SAE) for nanowire growth because

the engineered placement of nanowires, e.g., identical periodicity,³⁹⁻⁴¹ results in almost identical optical absorption for each nanowire in the array (except the nanowires close to the edges of array where periodicity fails). Again, by using our 3-D computational transient model, we have quantitatively studied the impact of each material property on τ_n and the carrier dynamics, and reconstructed real-time carrier dynamics in those 3-D structures. We believe this work will trigger additional experimental and theoretical work and unveil the real strength of TRPL for exploring carrier dynamics in nanowires and nanostructured materials.

Simulation and experimental section

Instruction of 3-D transient model

Our 3-D computational transient model of nanowire was set up by Synopsys[®] Sentaurus TCAD to mimic a TRPL measurement process. The output of the simulation is the temporal optical emission from band-to-band radiative recombination, i.e., emission intensity as a function of time, in response to a picosecond laser pulse. A diagram of the simulation process composed of three major steps is shown in Fig. 1. First, we constructed a unit cell including a nanowire, dielectric mask, substrate, and ambient air. The dimensions of the nanowire, i.e., height and diameter, can be defined by either scanning electron microscope (SEM) or cross-sectional transmission electron microscopy (TEM) measurements. Then, we computed the optical generation (in units of $\text{cm}^{-3}\text{s}^{-1}$) in the nanowire using normally incident light by finite-difference time-domain (FDTD). Next, by combining the Poisson equation, current-density equation, and continuity equation in the transient model, we calculated the temporal band-to-band radiative recombination in a nanowire segment by coupling temporal optical generation. To reproduce the TRPL measurement, we specified time dependency for transient simulations by setting the optical signal profile as a Gaussian function to mimic a picosecond laser pulse. As mentioned above, three types of material properties were set as variables: mobility (μ), SRH recombination lifetime (τ_{SRH}), and surface recombination velocity (S_n) at the interface with the substrate. More explanation of material properties will be given later. Finally, carrier lifetime τ was extracted by fitting to an exponential equation with a

single decay $\exp(-t/\tau)$. We computationally mapped the spatial and temporal carrier distributions in nanowire segments to reveal the underlying carrier dynamics. Note that we used a low excitation condition in simulations and thus the lifetime τ was minority carrier lifetime.

A case of GaAs nanowires on Si

To experimentally validate the 3-D TRPL transient model, we study the case of p-type GaAs nanowires grown on p-type Si substrates. The lattice mismatch between GaAs and Si is about 4.1%, and electrons were considered the minority carriers. We first performed a series of growths of Zn-doped GaAs nanowires on lightly boron-doped Si (111) wafers by selective-area metal-organic chemical deposition (SA-MOCVD). The diameter and pitch of the nanoholes were 80 nm and 800 nm, respectively, defined by electron-beam lithography (EBL). The size of the arrays was designed as $50 \times 50 \mu\text{m}^2$, much larger than the laser spot size. Prior to the growth of the nanowire segment, a thin GaAs seeding layer was introduced as a buffer to achieve high vertical yield and high uniformity across the nanowire array. To vary the GaAs-Si heterointerface material quality, five different growth temperatures for the seeding layers (T_{Seed})—450°C, 550°C, 600°C, 625°C, and 650°C—were used, while the nanowire growth temperature remained fixed at 730°C. The nanowires were passivated *in-situ* by a lattice-matched AlGaAs shell followed by a thin GaAs shell to reduce surface recombination at the semiconductor-to-air interface. We have labelled these five samples according to different seeding layer growth temperatures: Sample A (450°C), Sample B (550°C), Sample C (600°C), Sample D (625°C), and Sample E (650°C), respectively. More details of nanowire growth are given in the ESI.†

Next, the minority (electron) carrier lifetimes (τ_n) of Samples A to E for band-to-band recombination (875 nm) were carried out by TRPL at room temperature (300 K) using a pulsed laser operated at 633 nm with a repetition rate of 40 MHz and a pulse width of 30 ps. The lifetimes were taken on the as-grown nanowire arrays. The laser power density was calibrated to 178 W/cm². Note that the laser pump power was kept relatively low in order to consider electrons as minority carriers. As shown in the later discussion (in Fig. 8), the density of excess electrons is about $1 \times 10^{16} \text{ cm}^{-3} - 1 \times 10^{17} \text{ cm}^{-3}$, and thus

filling of traps was not likely. The measured TRPL curves are shown in Fig. 2, and the extracted τ_n as a function of T_{Seed} is summarized in the inset. To obtain τ_n , the TRPL curves between 0.4 ns and 1.4 ns were fitted by a single exponential decay expressed as $exp(-t/\tau)$. The calculated τ_n of Samples A to E were 0.52 ns, 0.84 ns, 1.25 ns, 0.73 ns, and 0.60 ns, respectively. Further details of optical characterization are given in the ESI.†

Model setup

Recall that the entire simulation started with the construction of a 3-D model based on actual nanowire dimensions. Thus, we first measured the dimensions—height and diameter—of Samples A through E by SEM, and investigated the cross-sections of nanowires by TEM. A 30°-tilted SEM image of GaAs nanowire array Sample C (600°C) is shown in Fig. 3(a). More SEM images of other samples can be found in Fig. S2 (ESI†). Clearly, Samples B through D show high vertical yield—nearly 100% for Samples B and C and over 85% for Sample D—similar to the growth of un-doped GaAs nanowires by SA-MOCVD.⁴² In contrast, Samples A and E show a much lower vertical yield with some randomly located irregular polycrystalline structures and tilted nanowires. The average height and diameter of the vertical nanowires are 740 nm and 135 nm, respectively, as shown in Fig. S3 (ESI†) – all samples show a good uniformity, with a variation of no more than 6 nm. Sample C (600°C) was prepared for TEM analysis by focus ion beam (FIB) milling, and an FEI T12 TEM was operated in bright field to study the GaAs-Si heterointerface regions and the GaAs nanowire segments, as shown in Fig. 3(b). Crystal defects—zinc-blende (ZB)–wurtzite (WZ) polytypisms and stacking faults—were observed, which was expected in patterned SAE growth of III-V nanowires. Interestingly, the seeding layer growth was initiated beneath the SiN_x growth mask, and a trapezoid-shaped GaAs crystalline structure was formed, with a thickness of 6 nm to 7 nm (more details in the ESI†). It was expected that the GaAs seeding layer would fill up to the top of the SiN_x mask, as shown in a previous study for InGaAs nanowire growth on Si with GaAs stub (Fig. S6, Ref. 7). Thus, the growth beneath the mask was included in the 3-D model.

A cross-sectional schematic diagram of the 3-D model composed of a GaAs nanowire and Si substrate is illustrated in Fig. 3(c), along with a close-up look of the seeding layer segment and GaAs-Si heterointerface. The dimensions characterized by TEM are labelled. No threading dislocations or antiphase domains (APDs) were found at GaAs-Si heterointerfaces. To simplify the simulation structure, we made several assumptions. First, the nanohole and trapezoid-shaped segments were fully covered by GaAs seed, and their geometries were approximated as cylindrical, which was similar to the GaAs stubs shown in a previous work (Fig. S6, Ref. 7). Second, since the thickness of the AlGaAs passivation layer was estimated as only 5 nm to 10nm, it was not included in the schematics; instead, we simplified its structure by introducing surface recombination velocity at GaAs/air interfaces on six (110) sidewalls of GaAs nanowires. The energy-band diagram as well as the quasi-Fermi level of the segment along the GaAs-Si heterointerface is schematically shown in Fig. 3(c) as well, and the interface states, i.e., traps, that result in nonradiative recombination are illustrated.

Optical simulation

After building the 3-D geometry, we moved on to the optical simulation. To precisely replicate the TRPL measurement in the simulation, we defined the optical wavelength as 633 nm and the optical power density as 178 W/cm². Periodic boundary conditions were used in X and Y directions, while perfectly matched layer absorbing boundary was used in Z direction. Fig. 4 shows the simulated optical generation along the cross-section of nanowire (Y-Y plane). Compared with GaAs segments, optical absorption in the Si substrate was much less due to its smaller absorption coefficient. Note that the photogenerated carriers were mostly concentrated in the top and bottom regions of the nanowire as well as the area near the GaAs-Si heterointerface. This can be explained by optical resonant-guided modes that increase the electromagnetic field intensity resulting from the coupling of the normally incident light to low-Q modes of the periodic 3-D structures, which is essentially different compared with any thin-films.

Electrical transient simulation and material parameters

The last step was to perform transient simulations of band-to-band radiative recombination of GaAs segments (including GaAs seeding layers) at 875 nm by coupling drift-diffusion and continuity equations with optical generation solved by FDTD. Since the repetition rate of laser pulse was 40 MHz, far beyond the time required for the system to revert to equilibrium, we only simulated one cycle of TRPL. To reproduce a transient process, we treated the temporal profile of the ‘laser beam’ as a Gaussian distribution — the pulse peaked at 60 ps and the pulse width was defined as 30 ps.

As mentioned above, three types of material properties were included in the model: mobility (μ), SRH recombination lifetime (τ_{SRH}), and surface recombination velocity (S_n) at the interface. Therefore, there were five variables in total: the electron mobility of the nanowire (μ_{n_wire}) and the seeding layer (μ_{n_seed}), the SRH recombination lifetime of the nanowire (τ_{SRH_wire}) and the seeding layer (τ_{SRH_seed}), and surface recombination velocity (S_{n_hetero}) at GaAs-Si heterointerface. The material properties of Samples B to D will be determined later by fitting to the experimental TRPL curves in Fig. 2. Samples A and E were not included in the transient simulations due to their low vertical yield, where the optical periodic boundary conditions no longer apply. The randomly located irregular polycrystalline structures and tilted nanowires shown in Fig. S2 were attributed to the formation of multiple types of nucleation during seeding layer growth (more details in the ESI†).⁴³ Therefore, it was fair to expect that the material quality of seeding layers grown at different temperatures varied. Additionally, crystal defects were clearly observed by TEM, and thus the electron mobility of these GaAs nanowires was expected to be much lower than that of thin-film GaAs or VLS GaAs nanowires due to stronger scattering.

Based on an intuitive understanding of material properties and their qualities, we set the values of each material property as follows to fit TRPL curves: (1) electron mobility of nanowire μ_{n_wire} 10 – 500 $\text{cm}^2/(\text{V}\cdot\text{s})$, (2) electron mobility of seeding layer μ_{n_seed} 0.5 – 10.0 $\text{cm}^2/(\text{V}\cdot\text{s})$, (3) SRH recombination lifetime of nanowire τ_{SRH_wire} 1.0 ns – 5.0 ns, (4) SRH recombination lifetime of seeding layer τ_{SRH_seed} 0.1 ns – 1.0 ns, and (5) surface recombination velocity at the nanowire-substrate heterointerface S_{n_hetero} $1.0\times 10^0 \text{ cm/s} - 1.0\times 10^6 \text{ cm/s}$. Note that the nonradiative SRH recombination lifetime was considered as a

variable, while a constant radiative recombination coefficient of $2.0 \times 10^{-10} \text{ cm}^3/\text{s}$ was applied to both the nanowire and the seeding layer segments. Additionally, Auger recombination was not significant due to a low level of incident laser power. The hole mobility (μ_p), i.e., the mobility of the majority carrier, was set as 10 times less than the electron mobility (μ_n) (a default setting). The surface recombination velocity at the nanowire-air interface (S_{n_air}), i.e., at the GaAs/AlGaAs heterointerface, was fixed at $1.0 \times 10^3 \text{ cm/s}$, based on the suggested values in some published studies.^{23, 28} All other material parameters were set as default values offered by the material database in the simulator.

Results and discussion

Minority carrier lifetimes by TRPL measurements

Compared with the reported studies of intrinsic GaAs nanowires on Si,^{27, 44} the Zn-doped GaAs with a 600°C seeding layer (Sample C) shows a comparable minority carrier lifetime (τ_n) of 1.25 ns. Clearly, τ_n is largely affected by the seeding growth temperature (T_{Seed}), as shown in the inset of Fig. 2. Here, we note a rapid decrease of τ_n from 1.25 ns to a much lower value less than 1 ns while T_{Seed} is away from 600°C, which might be due to an increase of local defect density inside the GaAs seeding layer or at the GaAs-Si heterointerface. As expected, τ_n has a positive correlation with the vertical yield of nanowires because intuitively speaking, τ_n of individual irregular polycrystalline structures should be shorter. Further, it is found that although the growth yield and uniformity of Samples B and C are comparable, the carrier lifetimes are much different. Thus, we suspect that the quality of GaAs seeding layers have an impact on the material properties of the upper GaAs segments – which is a fair assumption for heteroepitaxy. This fact, in turn, supports our core argument that the measured lifetime is a convolution of multiple recombination mechanisms which cannot be simply deconvolved without detailed analysis of 3-D carrier dynamics. In the transient simulations, we take this aspect into account by varying the properties of seeding layers and nanowire segments simultaneously.

Impacts of material properties on carrier lifetime

To study the impact of material properties on carrier lifetime, we first investigate the contributions from nanowire electron mobility μ_{n_wire} ($10 - 500 \text{ cm}^2/[\text{V}\cdot\text{s}]$) as well as surface recombination velocity at the GaAs-Si heterointerface S_{n_hetero} ($1.0 \times 10^0 \text{ cm/s} - 1.0 \times 10^6 \text{ cm/s}$) while τ_{SRH_wire} (5 ns) and τ_{SRH_seed} (1 ns) are kept fixed. Since the GaAs seeding layer was grown at a much lower temperature, we expect that the material quality of the seed would be much different from that of the nanowire, which is similar to the case for thin-film low-temperature GaAs (LT-GaAs). As a starting point, we assume μ_{n_seed} ($1 - 50 \text{ cm}^2/[\text{V}\cdot\text{s}]$) is one tenth of μ_{n_wire} ($10 - 500 \text{ cm}^2/[\text{V}\cdot\text{s}]$). Fig. 5(a) shows a contour plot of τ_n as a function of μ_{n_wire} and S_{n_hetero} , which is also marked by three contour lines at 0.84 ns, 1.25 ns, and 0.73 ns, corresponding to the measured τ_n of Samples B through D, respectively. Note that by only changing S_{n_hetero} , τ_n cannot vary from 0.73 ns to 1.25 ns. This is a crucial signal indicating that other material properties apart from S_{n_hetero} must be concurrently changed while the seeding layer growth temperature is altered. More simulated τ_n corresponding to other material properties will be given in the later discussion.

The variation of τ_n due to electron mobilities is remarkable – the value spans from 0.029 ns to 2.042 ns with S_{n_hetero} of $1.0 \times 10^0 \text{ cm/s}$ while it varies from 0.027 ns to 1.876 ns with S_{n_hetero} of $1.0 \times 10^6 \text{ cm/s}$. It is observed that the change of τ_n exhibits more significant dependency on electron mobility than on surface recombination velocity at the heterointerface. With larger mobility, the diffusion of electrons will be enhanced, which can be explained by the Einstein relation $D_n = \mu_n k_B T$, where D_n is the diffusivity of electrons, k_B is the Boltzmann constant, and T is the lattice temperature. Due to the large surface-to-volume ratio of nanowires, the carriers are likely to recombine at the nanowire sidewalls before diffusing to the GaAs-Si heterointerfaces, and thus the nonradiative recombination at the GaAs-Si heterointerfaces is not a dominant contributor to carrier dynamics. Nonetheless, this might not be the case if the aspect ratio of the nanowire, i.e., the ratio of height to diameter, is lower, or the diameter of nanohole is larger, where the probability for carriers is higher to reach heterointerfaces. Fig. 5(b) illustrates the simulated TRPL curves, i.e., radiative recombination of GaAs as a function of time, with a constant S_{n_hetero} of $1.0 \times 10^0 \text{ cm/s}$ and a series of μ_{n_wire} from $10 \text{ cm}^2/(\text{V}\cdot\text{s})$ to $75 \text{ cm}^2/(\text{V}\cdot\text{s})$. The intensity of emission reaches a maximum at 60 ps and starts to decay along with carrier diffusion and recombination. The overall τ_n

varies from 2.04 ns to 0.55 ns, which reveals the large impact of electron mobility on carrier recombination. Note that the change in τ_n is almost negligible while S_{n_hetero} varies within 1.0×10^0 cm/s – 1.0×10^3 cm/s, only becoming noticeable with larger S_{n_hetero} , suggesting that nonradiative recombination at heterointerfaces is dominant compared to recombination at other surfaces.

So far, we have fixed τ_{SRH_wire} at 5 ns and τ_{SRH_seed} at 1 ns, which would presumably be high for GaAs nanowires grown on Si substrates. Interestingly, we find that τ_n can be as low as tens of ps with high carrier mobility and significant carrier diffusion. Therefore, observing a short carrier lifetime in nanowires does not necessarily mean that the actual radiative/nonradiative lifetimes are short or material properties are imperfect—the impacts of carrier mobility, nonradiative recombination at surfaces, as well as 3-D geometry (surface-to-volume ratio) must be taken into account, and can only be deconvolved using a computational 3-D model. Based on the results given in Fig. 5, it is fair to assume that the simulated τ_n with S_{n_hetero} of 1.0×10^0 cm/s sets the upper limit, and the actual τ_n would be shorter due to smaller values of actual τ_{SRH_wire} and τ_{SRH_seed} . Since μ_{n_wire} yields a mobility of 10 – 75 cm²/(V·s) (more likely toward 10 cm²/(V·s)), we fix the value at 25 cm²/(V·s) in the next step, which is close to a reported carrier mobility of 31 cm²/(V·s) for p-type GaAs nanowires.⁴⁵ Indeed, we raise a concern in a previous section that the quality of seeding layers might affect the material properties of GaAs nanowires, meaning that μ_{n_wire} might not be a constant in Samples B to D. Still, we intentionally keep μ_{n_wire} fixed for the remaining simulations for the following reasons. First, the carrier mobility of III-V nanowires is predominantly determined by the density of polytypisms and stacking faults, which is found to be related to the growth temperature for selective-area GaAs nanowires. Since the nanowire segments are grown at the same temperature (730°C),⁴⁶ it is reasonable to assume the carrier mobility remains the same as well. Second, it is computationally easier to fix μ_{n_wire} in order to unveil the correlations between τ_n and other material properties.

Next, we vary four other material properties: τ_{SRH_wire} (1 ns – 5 ns), τ_{SRH_seed} (0.1 – 1.0 ns), S_{n_hetero} (1.0×10^0 cm/s – 1.0×10^6 cm/s), and μ_{n_seed} (0.5 – 10 cm²/(V·s)). Fig. 6(a) shows four 3-D contour plots of τ_n as a function of τ_{SRH_wire} , τ_{SRH_seed} , and S_{n_hetero} with a constant μ_{n_seed} of 0.5 cm²/(V·s), 1.0 cm²/(V·s), 5.0

$\text{cm}^2/(\text{V}\cdot\text{s})$, and $10.0 \text{ cm}^2/(\text{V}\cdot\text{s})$, respectively. Similar to the previous case, increasing μ_{n_seed} results in a decrease of τ_n , suggesting that carriers tend to diffuse a longer distance to the GaAs-Si heterointerface and then recombine. As for SRH recombination, τ_{SRH_wire} has a larger impact on τ_n than τ_{SRH_seed} , which is because the nanowire segment carries more minority carriers due to its larger spatial volume than the seeding layer. As for S_{n_hetero} , it barely affects τ_n while it is smaller than $1.0 \times 10^4 \text{ cm/s}$; however, its impact on τ_n becomes more significant when the value is larger than $1.0 \times 10^4 \text{ cm/s}$.

To further investigate the correlation between τ_n and material properties, we resummaries the lifetime information from each contour plot in Fig. 6(a) and replot it in box charts, as shown in Fig. 6(b). Each box (shown in green) in Fig. 6(b) presents a range of τ_n while altering τ_{SRH_seed} (1 ns – 5 ns) and S_{n_hetero} ($1.0 \times 10^0 \text{ cm/s}$ – $1.0 \times 10^6 \text{ cm/s}$) and keeping τ_{SRH_wire} and μ_{n_seed} fixed. In other words, the box offers estimated values of τ_n for different growth conditions of the GaAs seeding layer and the GaAs-Si heterointerface. Moreover, each box chart is labeled with three dashed lines, showing the boundaries of measured τ_n , i.e., 1.25 ns, 0.84 ns, and 0.73 ns, of Samples B to D. Clearly, with decreasing μ_{n_seed} , τ_n is more sensitive to the local nonradiative recombination in seeding layers and nanowire segments due to a less significant diffusion of carriers. Additionally, with longer τ_{SRH_wire} , it is more likely that electrons in the nanowire segments can diffuse into the seeding layer before being recombined – the overall τ_n exhibits more dependency on material properties of the seeding layer. Thus, we once again conclude that τ_n is not positively correlated to the material quality of either seeding layer or nanowire segment. Without determining the carrier mobility, it is nonsensical to attribute measured lifetime to any recombination mechanisms.

We further note that no single box in those four charts is able to cover a full range of τ_n from 0.73 ns to 1.25 ns, meaning that τ_n cannot be varied from 0.73 ns to 1.25 ns by changing either τ_{SRH_seed} or S_{n_hetero} . In other words, the variation of lifetime between Samples B to D cannot be simply attributed to a difference in GaAs-Si heterointerface quality – other material properties contribute as well. It is highly possible that the quality of the GaAs seeding layer has a significant impact on the upper GaAs segment—the material quality of the nanowire is concurrently degraded while the growth temperature of the seeding

layer is lower or higher than 600°C. Although the growth conditions, i.e., growth temperature, growth time, and gas flows, of nanowire segments for Samples A to E are consistent, local defects might be introduced at the seed-nanowire interface and then affect the growth quality of nanowire segments, which eventually causes a difference in nonradiative recombination mechanism in nanowire segments. Note that the seeding layer acts as a buffer layer between the lattice mismatched GaAs nanowires and Si substrates. It is well known that the quality of this buffer layer affects the quality of the material grown atop in thin-film epitaxy (e.g. GaAs grown on Si(001))⁴⁷⁻⁴⁹ – the same should apply to nanowires.

Final fitting of material properties

Equipped with the insights into recombination mechanisms of carriers, we now perform a numerical analysis to estimate reasonable values of τ_{SRH_wire} , τ_{SRH_seed} , S_{n_hetero} and μ_{n_seed} . As shown in Fig. 6(b), with $\mu_{n_seed} = 10.0 \text{ cm}^2/(\text{V}\cdot\text{s})$, τ_n cannot be over 1.25 ns, indicating that the actual mobility of all those samples should be lower. To cover a span of τ_n from 0.73 ns to 1.25 ns, the ranges of τ_{SRH_wire} should be within 1.2 ns and 2.3 ns, 1.4 and 2.5 ns, or 1.4 and 4.0 ns for $\mu_{n_seed} = 0.5 \text{ cm}^2/(\text{V}\cdot\text{s})$, $1.0 \text{ cm}^2/(\text{V}\cdot\text{s})$, or $5.0 \text{ cm}^2/(\text{V}\cdot\text{s})$, respectively. We expect that the material quality of both the nanowire and seeding segments of Sample C is the best among all samples. Thus, it is desired that the line of 1.25 ns crosses the top portion of the box where τ_{SRH_seed} is high and S_{n_hetero} is low, while the bottom boundary of 0.73 ns intersects the bottom part of the box. It is more likely that μ_{n_seed} is less than $5.0 \text{ cm}^2/(\text{V}\cdot\text{s})$, because we expect that the change of τ_{SRH_wire} resulting from the seeding layer growth temperature is significant and might be around 1 ns or so. A complete table that lists the simulated τ_n as a function of material properties is given in the ESI.†

Based on these assumptions, we suggest values for each material property, as listed in Table 1. Fig. 7 illustrates the simulated TRPL curves that fit experiments (in Fig. 2) by using suggested values listed in Table 1. It is clear that the measured τ_n shows a strong dependency on not only one but several recombination mechanisms. Since the carrier mobilities and radiative recombination rate are kept fixed for Samples B to D, we can safely assume that the radiative recombination lifetimes of those samples are approximately the same. As a result, the major recombination mechanisms that lead to the change of τ_n

are all attributed to nonradiative recombinations due to trap/defect states at GaAs-Si heterointerfaces and AlGaAs-GaAs surfaces, and within nanowire. Further, the probability of carriers being recombined also depends on the actual 3-D geometry of nanowire. Thus, we demonstrate here that the lifetime and material properties of a 3-D nanowire are certainly intercorrelated instead of in a simple one-to-one correlation.

3-D carrier dynamics

The temporal and spatial information of electron distribution provides a further insight into carrier motions and the recombination mechanisms of 3-D nanostructures. Thus, our final step is to show the capability of mapping real-time carrier dynamics using the 3-D transient model. The simulated spatial distributions of electrons at different points of time, i.e., 30 ps, 60 ps, 100 ps, 300 ps, 600 ps, and 1000 ps, for Samples B through D are illustrated in Fig. 7. At the initial stage, the density of photogenerated minority carriers keeps increasing when the samples are exposed under laser pulses from 10 ps to 60 ps. Then, from 60 ps to 1000 ps, electrons in the nanowire segments start to diffuse either toward the top or downward to the GaAs-Si heterointerfaces, while the density of electrons decreases due to nonradiative recombination within the nanowires or at the interfaces. Similarly, electrons in the Si substrate diffuse toward Si-SiN_x and GaAs-Si interfaces and are then recombined. It is obvious that, starting from 100 ps, the electron density inside the nanowire of Sample C is larger than that of Samples B and D, which is due to a longer τ_{SRH} . We also note that the electron density close to the GaAs-Si heterointerface decreases with increasing S_n from Sample C to Samples B and D. Due to the intrinsic large surface-to-volume ratio for nanowires, τ_n would be largely affected by aspects of the nanowire itself rather than the nanowire-substrate heterointerface, unless the recombination in the GaAs seeding layer or at the GaAs-Si heterointerface is dominant, which would surpass the recombination along the nanowire sidewalls. Another possible approach to make recombination at the GaAs-Si heterointerface more significant is to properly design the patterns of nanowire array or nanowire dimensions, which would result in optical generation mostly close to the heterointerfaces.

Conclusions

In summary, we investigated the feasibility of unveiling carrier dynamics of 3-D nanostructures using TRPL measurements combined with a 3-D computational transient model. Our goal, as emphasized throughout the study, is to provide a theoretical foundation to concurrently extract multiple material properties by fitting measured TRPL curves. The motivation for the numerical model is that the 3-D geometries of nanostructures result in more complicated mechanisms of carrier recombination than those in thin films and analytical solutions cannot be simply found. Without losing generality, we considered three material properties as variables, i.e., carrier mobility, SRH nonradiative recombination lifetime, and surface recombination velocity at heterointerfaces. To valid the model, we grew p-type GaAs nanowires on p-type Si by SA-MOCVD, and then fit the TRPL curves by tuning material properties. We observed that the seeding layers grown at different temperatures resulted in different material properties for nanowires, seeding layers, and GaAs-Si heterointerfaces. Finally, we suggested fitting values for material properties based on a complete set of transient simulations, and further interpreted the carrier dynamics by mapping spatial and temporal electron distributions. We believe the presented theoretical and experimental work will stimulate more validating studies to reveal the hidden power of TRPL for fundamental research on nanowires and nanostructured materials.

†Electronic Supplementary Information (ESI)

Additional information related to the experiments and simulations.

Corresponding Author

*Email: dingkun.ren@ucla.edu

Funding sources

The Air Force Office of Scientific Research (grant no. FA-9550-12-1-0052), the National Science Foundation (grant no. ECCS-1314253), the UC Laboratory Fees Research Program (grant no. 12-LR-238568), the United States Department of Defense (grant no. NSSEFF N00244-09-1-0091), and Sêr Cymru National Research Network in Advanced Engineering and Materials.

Competing financial interests

There are no conflicts of interest to declare.

Acknowledgements

We would like to acknowledge the user facilities – UCLA Nanoelectronics Research Facility as well as Integrated Systems Nanofabrication Cleanroom (ISNC) and Electron Imaging Center for NanoMachines (EICN) in California NanoSystems Institute (CNSI). We also gratefully acknowledge the support from the Air Force Office of Scientific Research (grant no. FA-9550-12-1-0052), the National Science Foundation (grant no. ECCS-1314253), the UC Laboratory Fees Research Program (grant no. 12-LR-238568), and the United States Department of Defense (grant no. NSSEFF N00244-09-1-0091). In addition, the authors would like to acknowledge the financial support provided by Sêr Cymru National Research Network in Advanced Engineering and Materials.

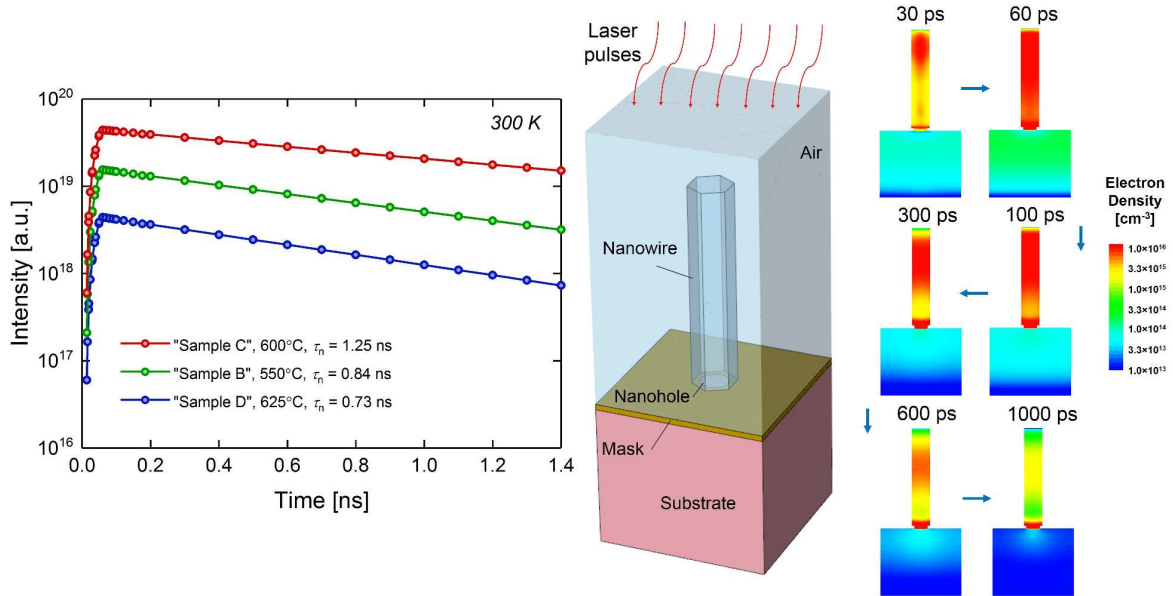
References

1. K. A. Dick and P. Caroff, *Nanoscale*, 2014, **6**, 3006-3021.
2. D. Ren, A. C. Farrell, B. S. Williams and D. L. Huffaker, *Nanoscale*, 2017, **9**, 8220-8228.
3. K. Tomioka and T. Fukui, *Applied Physics Letters*, 2011, **98**, 083114.
4. K. Tomioka, M. Yoshimura and T. Fukui, *Nature*, 2012, **488**, 189-192.
5. K. Tomioka, M. Yoshimura and T. Fukui, *Nano Letters*, 2013, **13**, 5822-5826.
6. B. Mayer, L. Janker, B. Loitsch, J. Treu, T. Kostenbader, S. Lichtmanecker, T. Reichert, S. Morkötter, M. Kaniber, G. Abstreiter, C. Gies, G. Koblmüller and J. J. Finley, *Nano Letters*, 2016, **16**, 152-156.
7. H. Kim, W.-J. Lee, A. C. Farrell, J. S. D. Morales, P. Senanayake, S. V. Prikhodko, T. J. Ochalski and D. L. Huffaker, *Nano Letters*, 2017, **17**, 3465-3470.
8. K. H. Li, LiuX, WangQ, ZhaoS and MiZ, *Nat Nano*, 2015, **10**, 140-144.
9. R. Chen, T.-T. D. Tran, K. W. Ng, W. S. Ko, L. C. Chuang, F. G. Sedgwick and C. Chang-Hasnain, *Nat Photon*, 2011, **5**, 170-175.
10. C. P. T. Svensson, M. Thomas, T. Johanna, L. Christina, R. Michael, H. Dan, S. Lars and O. Jonas, *Nanotechnology*, 2008, **19**, 305201.
11. K. Tomioka, J. Motohisa, S. Hara, K. Hiruma and T. Fukui, *Nano Letters*, 2010, **10**, 1639-1644.
12. W. Guo, M. Zhang, A. Banerjee and P. Bhattacharya, *Nano Letters*, 2010, **10**, 3355-3359.
13. N. Hieu Pham Trung, C. Kai, Z. Shaofei, F. Saeed and M. Zetian, *Nanotechnology*, 2011, **22**, 445202.
14. W. Guo, A. Banerjee, P. Bhattacharya and B. S. Ooi, *Applied Physics Letters*, 2011, **98**, 193102.
15. K. Tomioka, T. Tanaka, S. Hara, K. Hiruma and T. Fukui, *IEEE Journal of Selected Topics in Quantum Electronics*, 2011, **17**, 1112-1129.
16. N. Hieu Pham Trung, D. Mehrdad, C. Kai and M. Zetian, *Nanotechnology*, 2012, **23**, 194012.
17. M.-H. Bae, B.-K. Kim, D.-H. Ha, S. J. Lee, R. Sharma, K. J. Choi, J.-J. Kim, W. J. Choi and J. C. Shin, *Crystal Growth & Design*, 2014, **14**, 1510-1515.
18. E. Dimakis, U. Jahn, M. Ramsteiner, A. Tahraoui, J. Grandal, X. Kong, O. Marquardt, A. Trampert, H. Riechert and L. Geelhaar, *Nano Letters*, 2014, **14**, 2604-2609.
19. A. Brenneis, J. Overbeck, J. Treu, S. Hertenberger, S. Morkötter, M. Döblinger, J. J. Finley, G. Abstreiter, G. Koblmüller and A. W. Holleitner, *ACS Nano*, 2015, **9**, 9849-9858.
20. M. D. Thompson, A. Alhodaib, A. P. Craig, A. Robson, A. Aziz, A. Krier, J. Svensson, L.-E. Wernersson, A. M. Sanchez and A. R. J. Marshall, *Nano Letters*, 2016, **16**, 182-187.
21. J. C. Shin, K. H. Kim, K. J. Yu, H. Hu, L. Yin, C.-Z. Ning, J. A. Rogers, J.-M. Zuo and X. Li, *Nano Letters*, 2011, **11**, 4831-4838.
22. J. C. Shin, P. K. Mohseni, K. J. Yu, S. Tomasulo, K. H. Montgomery, M. L. Lee, J. A. Rogers and X. Li, *ACS Nano*, 2012, **6**, 11074-11079.
23. N. Jiang, P. Parkinson, Q. Gao, S. Breuer, H. H. Tan, J. Wong-Leung and C. Jagadish, *Applied Physics Letters*, 2012, **101**, 023111.

24. J. C. Shin, A. Lee, P. Katal Mohseni, D. Y. Kim, L. Yu, J. H. Kim, H. J. Kim, W. J. Choi, D. Wasserman, K. J. Choi and X. Li, *ACS Nano*, 2013, **7**, 5463-5471.
25. J. Wu, Y. Li, J. Kubota, K. Domen, M. Aagesen, T. Ward, A. Sanchez, R. Beanland, Y. Zhang, M. Tang, S. Hatch, A. Seeds and H. Liu, *Nano Letters*, 2014, **14**, 2013-2018.
26. M. Yao, S. Cong, S. Arab, N. Huang, M. L. Povinelli, S. B. Cronin, P. D. Dapkus and C. Zhou, *Nano Letters*, 2015, **15**, 7217-7224.
27. J. H. Kang, Q. Gao, P. Parkinson, H. J. Joyce, H. H. Tan, Y. Kim, Y. Guo, H. Xu, J. Zou and C. Jagadish, *Nanotechnology*, 2012, **23**, 415702.
28. N. Jiang, Q. Gao, P. Parkinson, J. Wong-Leung, S. Mokkaapati, S. Breuer, H. H. Tan, C. L. Zheng, J. Etheridge and C. Jagadish, *Nano Letters*, 2013, **13**, 5135-5140.
29. F. Wang, Q. Gao, K. Peng, Z. Li, Z. Li, Y. Guo, L. Fu, L. M. Smith, H. H. Tan and C. Jagadish, *Nano Letters*, 2015, **15**, 3017-3023.
30. P. Parkinson, H. J. Joyce, Q. Gao, H. H. Tan, X. Zhang, J. Zou, C. Jagadish, L. M. Herz and M. B. Johnston, *Nano Letters*, 2009, **9**, 3349-3353.
31. P. Parkinson, C. Dodson, H. J. Joyce, K. A. Bertness, N. A. Sanford, L. M. Herz and M. B. Johnston, *Nano Letters*, 2012, **12**, 4600-4604.
32. H. J. Joyce, P. Parkinson, N. Jiang, C. J. Docherty, Q. Gao, H. H. Tan, C. Jagadish, L. M. Herz and M. B. Johnston, *Nano Letters*, 2014, **14**, 5989-5994.
33. J. L. Boland, S. Conesa-Boj, P. Parkinson, G. Tütüncüoğlu, F. Matteini, D. Ruffer, A. Casadei, F. Amaduzzi, F. Jabeen, C. L. Davies, H. J. Joyce, L. M. Herz, A. Fontcuberta i Morral and M. B. Johnston, *Nano Letters*, 2015, **15**, 1336-1342.
34. M. M. Gabriel, J. R. Kirschbrown, J. D. Christesen, C. W. Pinion, D. F. Zigler, E. M. Grumstrup, B. P. Mehl, E. E. M. Cating, J. F. Cahoon and J. M. Papanikolas, *Nano Letters*, 2013, **13**, 1336-1340.
35. E. M. Grumstrup, M. M. Gabriel, E. E. M. Cating, E. M. Van Goethem and J. M. Papanikolas, *Chemical Physics*, 2015, **458**, 30-40.
36. E. M. Grumstrup, M. M. Gabriel, E. E. M. Cating, C. W. Pinion, J. D. Christesen, J. R. Kirschbrown, E. L. Vallorz, J. F. Cahoon and J. M. Papanikolas, *The Journal of Physical Chemistry C*, 2014, **118**, 8634-8640.
37. E. M. Grumstrup, M. M. Gabriel, C. W. Pinion, J. K. Parker, J. F. Cahoon and J. M. Papanikolas, *Nano Letters*, 2014, **14**, 6287-6292.
38. P. Parkinson, Y.-H. Lee, L. Fu, S. Breuer, H. H. Tan and C. Jagadish, *Nano Letters*, 2013, **13**, 1405-1409.
39. A. C. Scofield, J. N. Shapiro, A. Lin, A. D. Williams, P.-S. Wong, B. L. Liang and D. L. Huffaker, *Nano Letters*, 2011, **11**, 2242-2246.
40. P. Senanayake, C.-H. Hung, J. Shapiro, A. Lin, B. Liang, B. S. Williams and D. L. Huffaker, *Nano Letters*, 2011, **11**, 5279-5283.
41. G. Mariani, A. C. Scofield, C.-H. Hung and D. L. Huffaker, *Nat Communications*, 2013, **4**, 1497.
42. T. Katsuhira, K. Yasunori, M. Junichi, H. Shinjiroh and F. Takashi, *Nanotechnology*, 2009, **20**, 145302.
43. E. Russo-Averchi, M. Heiss, L. Michelet, P. Krogstrup, J. Nygard, C. Magen, J. R. Morante, E. Uccelli, J. Arbiol and A. Fontcuberta i Morral, *Nanoscale*, 2012, **4**, 1486-1490.

44. A. M. Munshi, D. L. Dheeraj, V. T. Fauske, D. C. Kim, J. Huh, J. F. Reinertsen, L. Ahtapodov, K. D. Lee, B. Heidari, A. T. J. van Helvoort, B. O. Fimland and H. Weman, *Nano Letters*, 2014, **14**, 960-966.
45. B. Ketterer, E. Uccelli and A. Fontcuberta i Morral, *Nanoscale*, 2012, **4**, 1789-1793.
46. J. N. Shapiro, PhD thesis, University of California, Los Angeles, 2013.
47. Q. Li, K. W. Ng and K. M. Lau, *Applied Physics Letters*, 2015, **106**, 072105.
48. T. Orzali, A. Vert, B. O'Brien, J. L. Herman, S. Vivekanand, R. J. W. Hill, Z. Karim and S. S. Papa Rao, *Journal of Applied Physics*, 2015, **118**, 105307.
49. R. Alcotte, M. Martin, J. Moeyaert, R. Cipro, S. David, F. Bassani, F. Ducroquet, Y. Bogumilowicz, E. Sanchez, Z. Ye, X. Y. Bao, J. B. Pin and T. Baron, *APL Materials*, 2016, **4**, 046101.

For Table of Contents Only



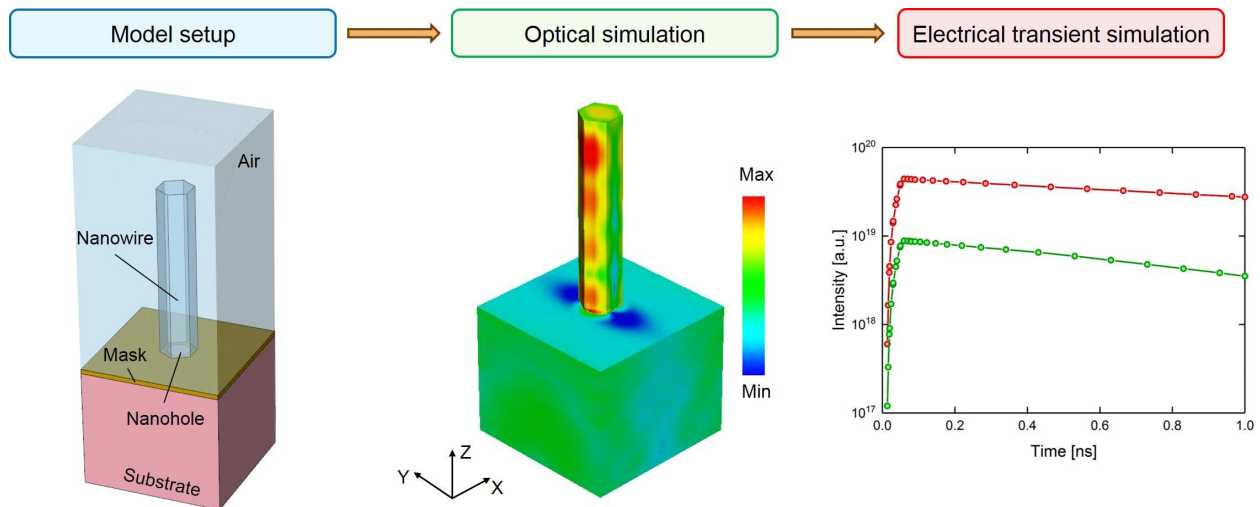


Fig. 1 Schematic diagram of simulation process composed of three major steps: (1) model setup, (2) optical simulation, and (3) electrical transient simulation.

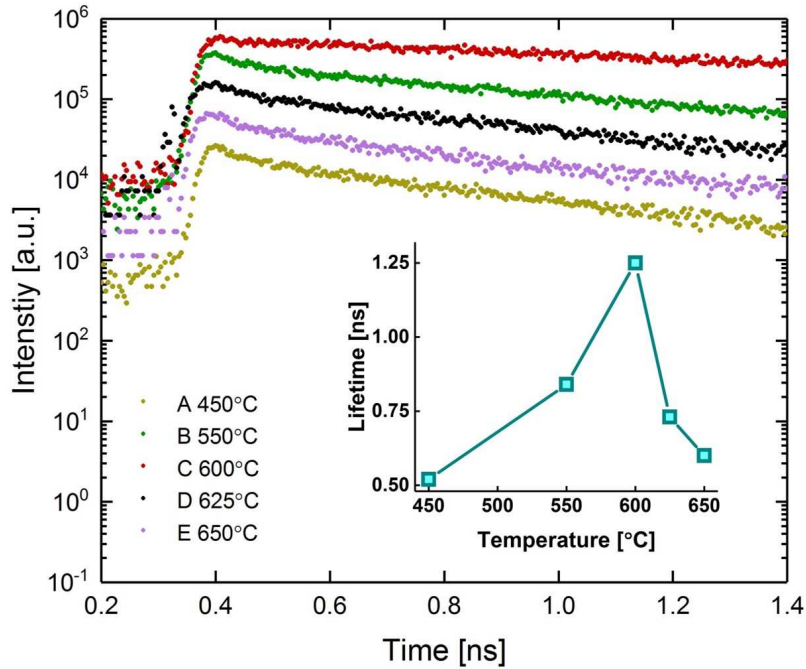


Fig. 2 The TRPL curves of Samples A to E at 300 K. The seeding layer growth temperatures of these three samples are 450°C, 550°C, 600°C, 620°C and 650°C, respectively. In the inset, the extracted lifetimes of Samples A to E are all given.

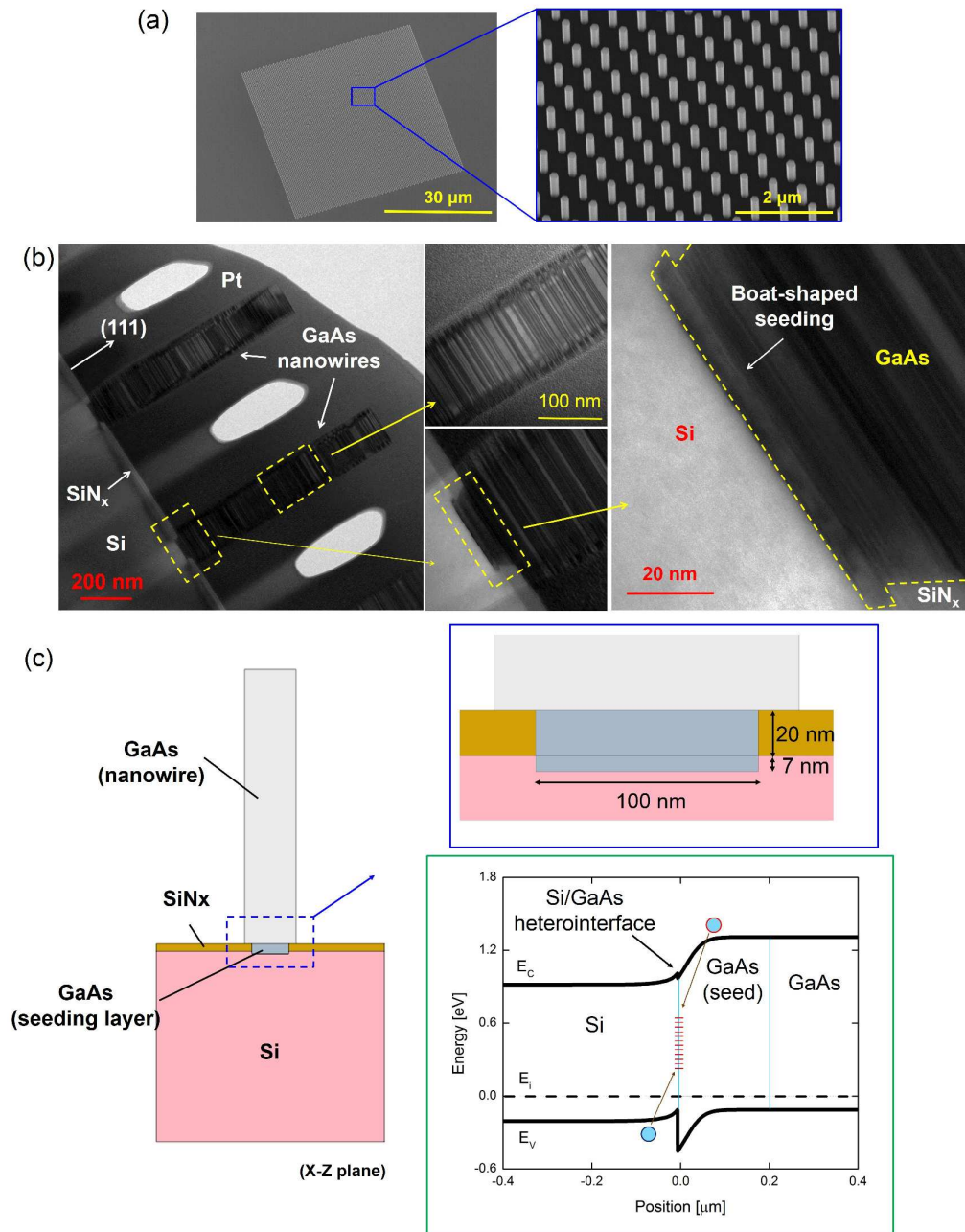


Fig. 3 (a) An as-grown $50 \times 50 \mu\text{m}^2$ array with extremely high uniformity. The GaAs seeding layer was grown at 600°C . The close-up image of nanowire array is shown on the right. (b) Cross-sectional TEM image of GaAs nanowires with GaAs seeding layer grown at 600°C . The two zoom-in images in the center show the nanowire segment and the trapezoid-shaped seeding layer. The further close-up detail of GaAs-Si interface is shown in the image on the right. (c) The cross-section of 3-D model showing the close-up of GaAs seeding layer and an energy-band diagram of GaAs-Si heterointerface. The interface states are illustrated.

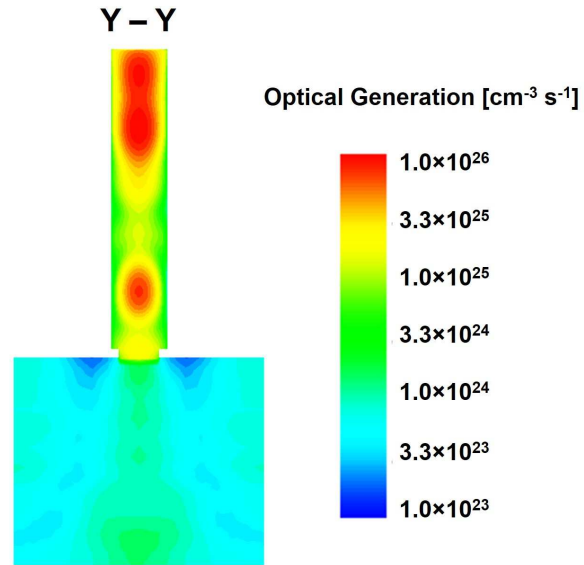


Fig. 4 FDTD simulation showing optical generation under top illumination at 633 nm with an incident power of 178 W/cm^2 .

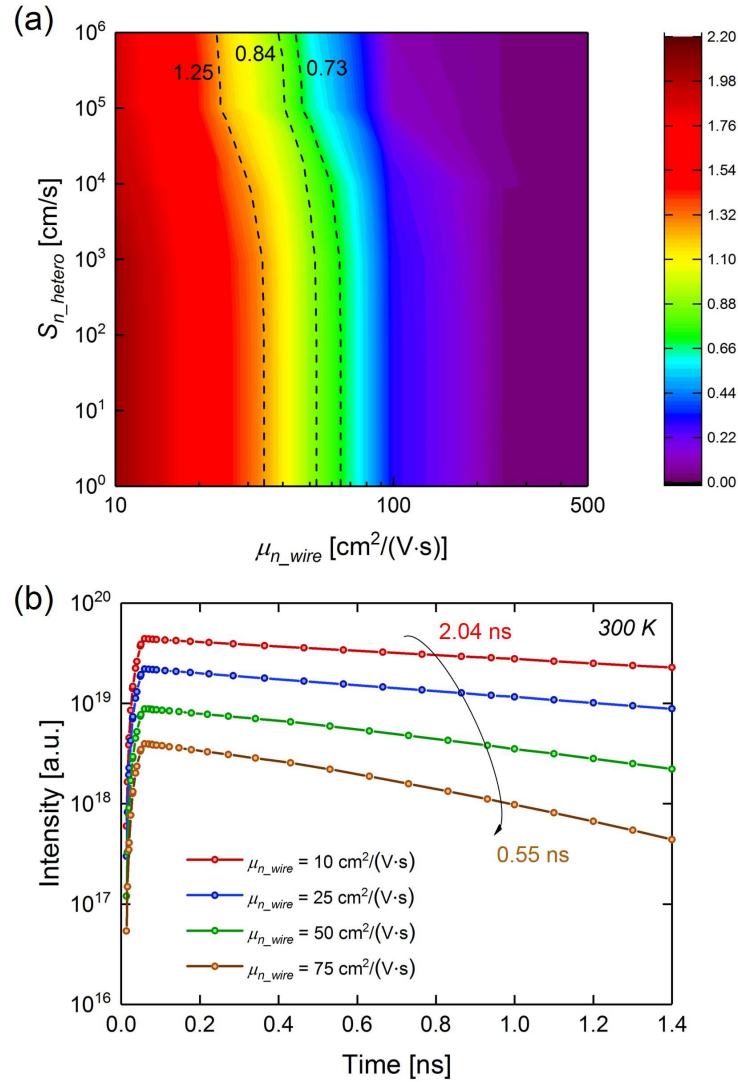


Fig. 5 Determining electron mobility of GaAs nanowire μ_{n_wire} . (a) Contour plot of simulated minority carrier lifetime τ_n as a function of μ_{n_wire} (10 – 500 $\text{cm}^2/(\text{V}\cdot\text{s})$) and S_{n_hetero} (10^0 – 10^6 cm/s). selective-area GaAs nanowires on Si for minority carrier lifetime simulation. Three contour lines correspond to the measured lifetime of Samples B to D: 0.73 ns, 1.25 ns, and 0.84 ns, respectively. (b) Simulated TRPL spectra at room temperature with different μ_{wire} of 10 $\text{cm}^2/(\text{V}\cdot\text{s})$, 25 $\text{cm}^2/(\text{V}\cdot\text{s})$, 50 $\text{cm}^2/(\text{V}\cdot\text{s})$, and 75 $\text{cm}^2/(\text{V}\cdot\text{s})$, which correspond to τ_n of 2.04 ns, 1.47 ns, 0.89 ns, and 0.55 ns, respectively. The values of other material properties used in the simulation are given: $\mu_{n_seed} = 0.1 \times \mu_{n_wire}$, $\tau_{SRH_wire} = 5$ ns, and $\tau_{SRH_wire} = 1$ ns.

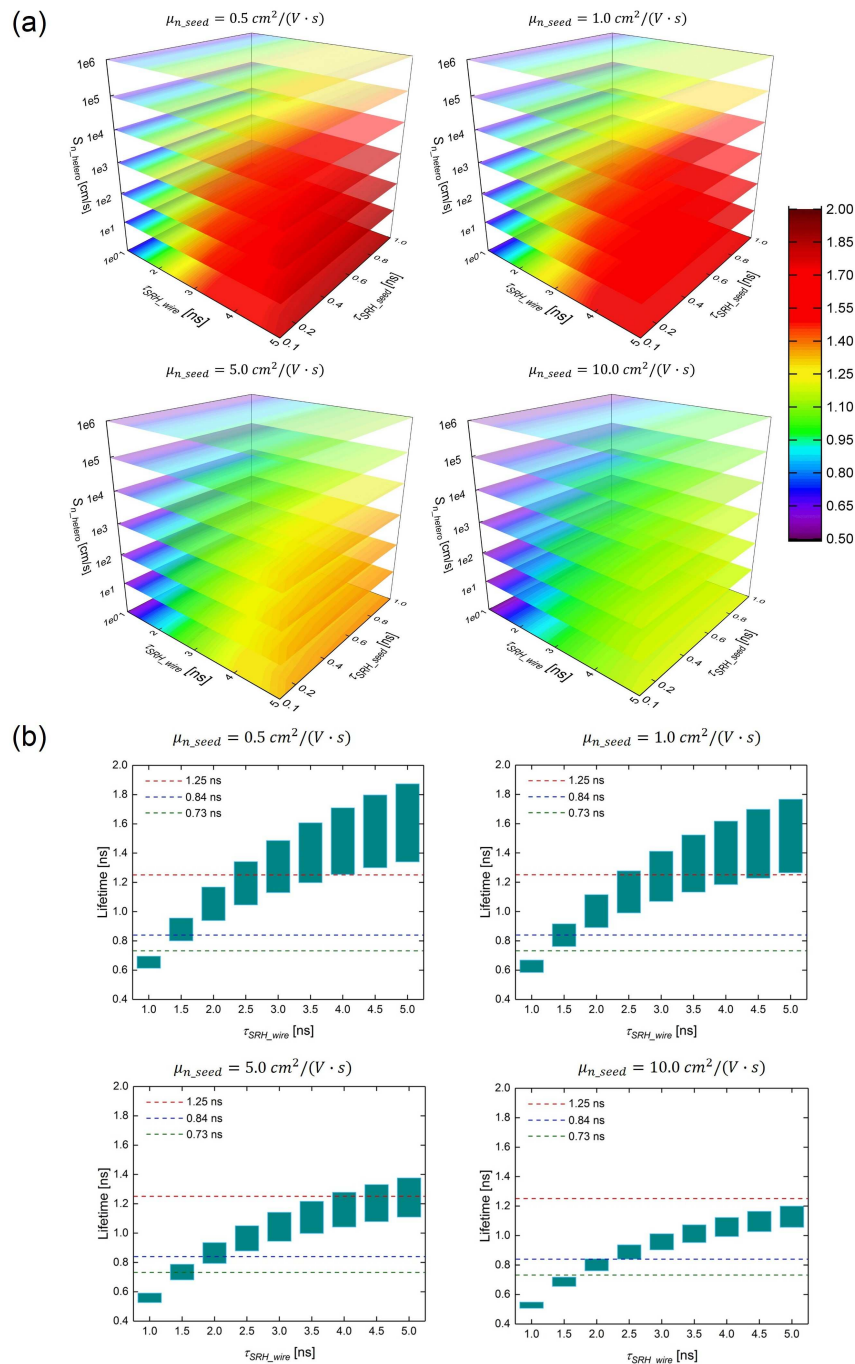


Fig. 6 The relation of minority carrier lifetime τ_n with other four material properties μ_{n_seed} , τ_{SRH_wire} , τ_{SRH_seed} , and S_{n_hetero} . (a) 3-D contour plots of simulated τ_n as a function of τ_{SRH_wire} (1 – 5 ns), τ_{SRH_seed} (0.1 – 1 ns), and S_{n_hetero} (10^0 – 10^6 cm^2/s). The electron mobility of seeding layer μ_{n_seed} (0.5 – 10.0 $cm^2/(V \cdot s)$) is fixed for each plot. (b) Box charts summarizing all possible values of τ_n as a function of τ_{SRH_wire} based on (a). Each box shows a range of τ_n by varying seeding layer properties τ_{SRH_seed} (0.1 – 1 ns) and S_{n_hetero} (10^0 – 10^6 cm^2/s).

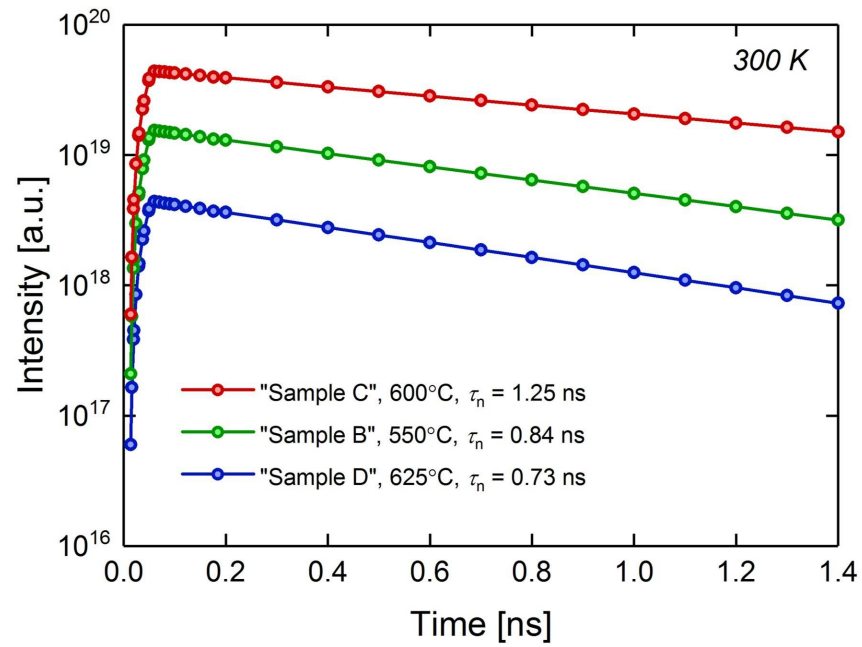


Fig. 7 Simulated TRPL spectra at room temperature with fitting values listed in Table 1.

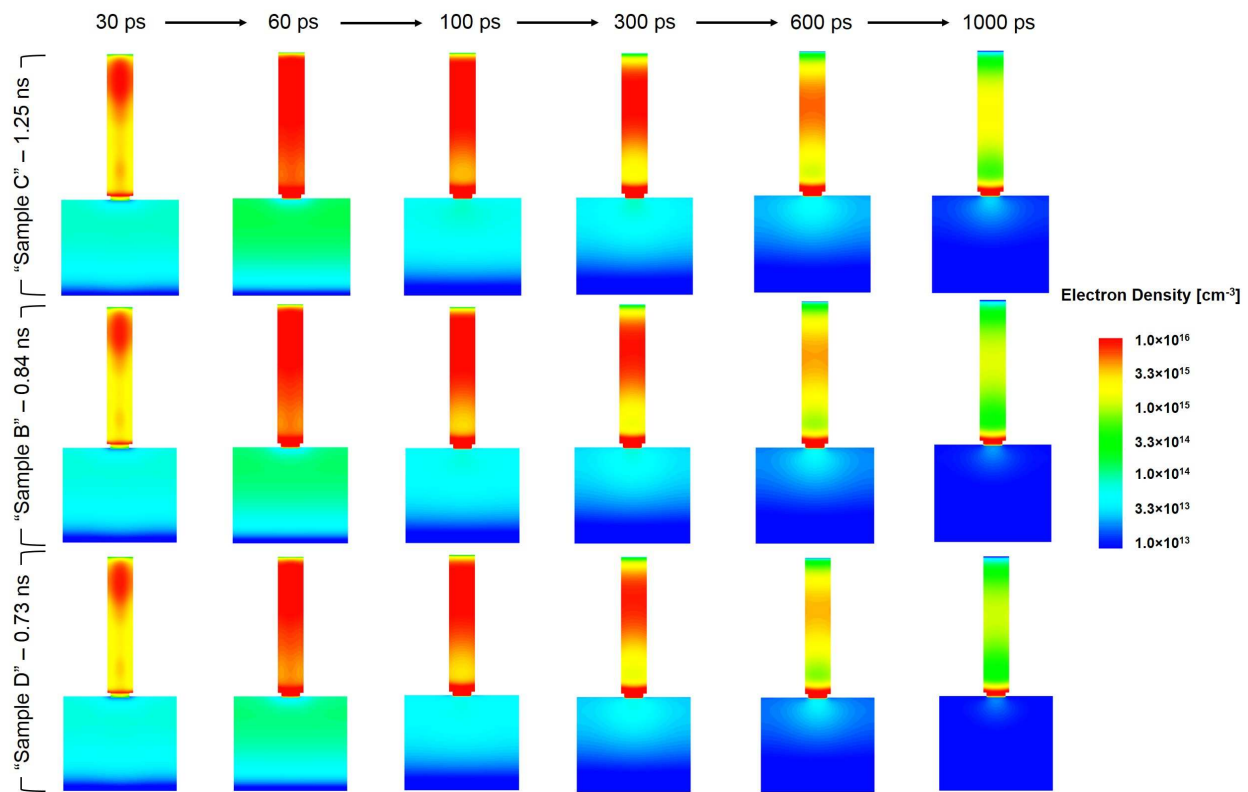
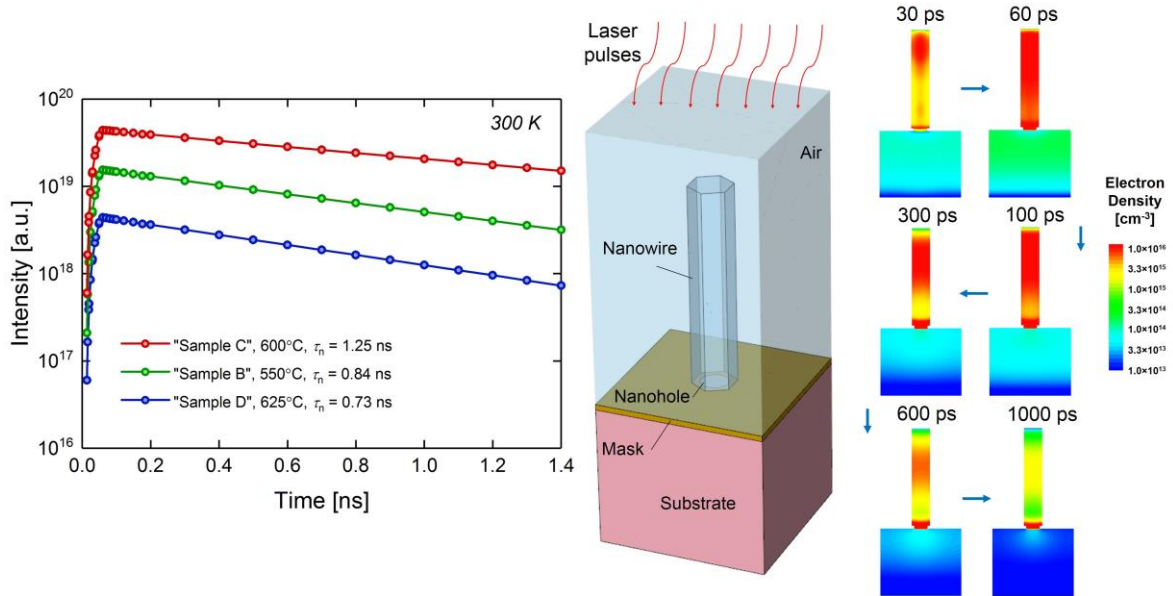


Fig. 8 Simulated spatial distribution of electrons at different points of time – 30 ps, 60 ps, 100 ps, 300 ps, 600 ps, and 1000 ps, respectively.

Table 1 Suggested fitting values of material properties for Sample B, Sample C, and Sample D

Sample	T_{Seed} [°C]	τ_n [ns]	μ_{n_wire} [cm ² /(V·s)]	μ_{n_seed} [cm ² /(V·s)]	τ_{SRH_wire} [ns]	τ_{SRH_seed} [ns]	S_n [cm/s]
B	550	0.73	25	1	1.5	0.2	1×10^5
C	600	1.25	25	1	2.5	0.3	1×10^2
D	625	0.84	25	1	1.4	0.1	1×10^4

Table of Contents Entry



Simulated time-resolved photoluminescence curves and temporal carrier distributions for GaAs nanowires on Si substrates.